Acta Crystallographica Section D
Biological Crystallography
ISSN 0907-4449

A functional and structural study of the major metalloprotease secreted by the pathogenic fungus *Aspergillus fumigatus*

Daniel Fernández,[a] Silvia Russi,[b] Josep Vendrell,[a] Michel Monod[c]* and Irantzu Pallarès[a]*

[a]Departament de Bioquímica i Biologia Molecular, Facultat de Biociències, Universitat Autònoma de Barcelona, 08193 Bellaterra, Spain, [b]Structural Biology Group, European Synchrotron Radiation Facility, 6 Rue Jules Horowitz, 38043 Grenoble, France, and [c]Service de Dermatologie et Vénéréologie, Laboratoire de Mycologie, BT422, Centre Hospitalier Universitaire Vaudois, 1011 Lausanne, Switzerland

Correspondence e-mail: michel.monod@chuv.ch, irantzu.pallares@uab.cat

Received 10 May 2013
Accepted 26 June 2013

PDB Reference: *A. fumigatus* metalloprotease, 4k90

Fungalysins are secreted fungal peptidases with the ability to degrade the extracellular matrix proteins elastin and collagen and are thought to act as virulence factors in diseases caused by fungi. Fungalysins constitute a unique family among zinc-dependent peptidases that bears low sequence similarity to known bacterial peptidases of the thermolysin family. The crystal structure of the archetype of the fungalysin family, *Aspergillus fumigatus* metalloprotease (AfuMep), has been obtained for the first time. The 1.8 Å resolution structure of AfuMep corresponds to that of an autoproteolyzed pro-enzyme with separate polypeptide chains corresponding to the N-terminal prodomain in a binary complex with the C-terminal zinc-bound catalytic domain. The prodomain consists of a tandem of cystatin-like folds whose C-terminal end is buried into the active-site cleft of the catalytic domain. The catalytic domain harbouring the key catalytic zinc ion and its ligands, two histidines and one glutamic acid, undergoes a conspicuous rearrangement of its N-terminal end during maturation. One key positively charged amino-acid residue and the C-terminal disulfide bridge appear to contribute to its structural–functional properties. Thus, structural, biophysical and biochemical analysis were combined to provide a deeper comprehension of the underlying properties of *A. fumigatus* fungalysin, serving as a framework for the as yet poorly known metallopeptidases from pathogenic fungi.

1. Introduction

Several species of *Aspergillus* are fungi that cause disease in domestic animals, cattle and humans. *Aspergillus* flourishes in a variety of environments and in decaying organic matter, such as in air-conditioning systems, building materials and indoor plant soil, producing huge quantities of airborne spores and hyphal fragments that can be inhaled. *Aspergillus* can be life-threatening in immunocompromised individuals such as transplant recipients and patients with haematologic malignancies. Three forms of disease have been recognized: allergic bronchopulmonary aspergillosis, aspergilloma (lung fungus ball disease) and invasive pulmonary or disseminated aspergillosis, which is the most severe and is associated with high morbidity and mortality rates in high-risk groups (Abad *et al.*, 2010; Dagenais & Keller, 2009; Hohl & Feldmesser, 2007; Latgé, 1999; McCormick *et al.*, 2010).

Among the various potential virulence factors proposed for pathogenic fungi, secreted proteolytic activity has attracted much attention. Various secreted proteases are synthesized as long prepropeptide immature enzymes that enter the secretory pathway and eventually acquire their mature state by endogenous (autoproteolytic) or exogenous cleavage of the

propeptide. Like many other ascomycete fungi, *A. fumigatus* secretes two major endoproteases: a subtilisin or **al**kaline **p**rotease (Alp; Monod *et al.*, 1991; Reichard *et al.*, 1990), which is very similar to other well characterized subtilisins, and a **me**tallo**p**rotease (Mep; Monod, Paris, Sanglard *et al.*, 1993) similar to bacterial metalloendopeptidases of the thermolysin family when grown in the presence of protein as the sole nitrogen source at a neutral pH. Δ*alp* Δ*mep* knockout mutants are unable to grow in a medium containing protein as the sole nitrogen source at neutral and alkaline pH, while single Δ*alp* and Δ*mep* mutants produced 30 and 70% of the proteolytic activity of the wild-type strain, respectively (Jaton-Ogay *et al.*, 1994, Monod, Paris, Sarfati *et al.*, 1993).

Mature AfuMep (*Aspergillus fumigatus* metalloprotease), a 42 kDa unglycosylated protein, was first isolated from Δ*alp* mutant cultures (Monod, Paris, Sanglard *et al.*, 1993). However, the protein is synthesized as a 68 kDa prepro-enzyme with a predicted signal sequence (residues 1–18) required for the secretory pathway, a long prodomain (19–245) and a catalytic core (246–634) that becomes separated from the propeptide after an autoproteolytic event. The 389-amino-acid catalytic domain displays the HE*XX*H signature of zinc in metallopeptidases and thus was predicted to have a fold similar to that of the members of the thermolysin family, despite a significantly low sequence identity (Sirakova *et al.*, 1994). AfuMep exhibits a preference for cleavage on the amino side of hydrophobic residues with bulky side chains and can hydrolyze elastin and collagen (Monod, Paris, Sanglard *et al.*, 1993; Sirakova *et al.*, 1994). It was shown to be competitively and specifically inhibited in the nanomolar range by its own propeptide previously obtained as a recombinant peptide in *Escherichia coli* (Markaryan *et al.*, 1996). AfuMep has maximal collagenolytic activity at basic pH, with a plateau between pH 7.0 and 9.0, and is strongly inhibited by divalent cations and by metal-chelating agents such as EDTA, 1,10-phenanthroline and phosphoramidon. The enzyme is thermosensitive and treatment with reducing agents such as β-mercaptoethanol and dithiothreitol abolishes its activity. AfuMep behaves as an antigenic protein that reacts positively with sera from aspergilloma patients whilst being unreactive to sera from healthy control individuals, suggesting that the enzyme may be secreted in substantial amounts *in vivo* (Monod, Paris, Sanglard *et al.*, 1993). In addition, immunogold electron microscopy localized this enzyme in the lung tissue of infected neutropenic mice (Markaryan *et al.*, 1994).

The fungalysins [MEROPS M36 family, clan MA, subclan MA(E); Rawlings *et al.*, 2012], of which AfuMep is the archetype, are primarily found in fungi as a single copy in *Aspergillus* species or as multiple copies in the dermatophytes *Microsporum canis*, *Trichophyton rubrum* and *T. mentagrophytes*, which are human and animal pathogenic fungi that cause cutaneous infections. The expansion of genes encoding fungalysins in dermatophytes correlates with their specialization and is often considered as a virulence trait as it occurs for other gene families in various fungi. The best example for secreted proteases is the human pathogenic yeast *Candida albicans*, which expresses different genes encoding closely related secreted aspartic proteases in reaction to specific environmental conditions during infection (Burmester *et al.*, 2011; Jousson *et al.*, 2004; Monod, 2008).

No tertiary structure is yet known for any fungalysin. To gain a deeper insight into the subject, we pursued a structural and functional study of an archetype of the family, *A. fumigatus* fungalysin. Crucially, its low overall sequence similarity to any protein with available three-dimensional structure made it an attractive target for a full X-ray crystallographic study. *A. fumigatus* Mep was expressed recombinantly and crystallized in a high-throughput setting. Native AfuMep crystals were derivatized with K_2PtCl_4 and the structure was solved by single-wavelength anomalous diffraction (SAD) from data collected at the Pt peak. The final model obtained at a resolution of 1.8 Å comprised the binary complex formed by the catalytic domain Zn^{2+} ion and the cleaved propeptide. This represents the first structural analysis of any metallopeptidase from the M36 family of fungalysins. The newly determined three-dimensional structure confirmed previous predictions inferred from biochemical and phylogenetic analyses regarding its similarity to the thermolysin family of peptidases. This notwithstanding, remarkable differences arose from our structural and biochemical data as will be reported herein.

2. Materials and methods

2.1. Enzyme production

A previously constructed *Pichia pastoris* transformant producing recombinant His_6-tagged *A. fumigatus* Mep was used (Sarfati *et al.*, 2006). The expression plasmid used for *P. pastoris* GS115 transformation was constructed by cloning *A. fumigatus* cDNA encoding Mep in the expression vector pKJ111 (Monod *et al.*, 1999). Likewise, various His_6-tagged mutated *A. fumigatus* Meps were obtained after transformation of *P. pastoris* GS115 with plasmid pKJ111 derivatives in which synthesized DNA coding for a mutated Mep (Genecust, Dudelange, Luxembourg) was inserted instead of DNA coding for wild-type Mep. The cloned inserts encoding all mutated Meps were checked *via* sequencing. *P. pastoris* transformation and selection of transformants were performed as described previously (Beggah *et al.*, 2000; Sarfati *et al.*, 2006). The different mutants were designed to produce either the non-autoproteolyzed inactive enzyme, namely His429Met, Glu430Ala and Glu459Met, or to analyze residues believed to be important for the structure such as Arg470, giving Arg470Ala, Arg470Glu, Arg470Ser and Arg470Lys, in addition to Cys634 (Cys634Ala).

For enzyme production, *P. pastoris* transformants were grown to near-saturation (OD_{600} = 10) at 303 K in 10 or 500 ml glycerol-based yeast medium (0.1 *M* potassium phosphate buffer pH 6.0 containing 10 g l^{-1} yeast extract, 20 g l^{-1} peptone, 13 g l^{-1} yeast nitrogen base without amino acids, 10 ml l^{-1} glycerol and 40 mg l^{-1} biotin). Cells were harvested and resuspended in 2 or 100 ml of the same medium with 5 ml l^{-1} methanol instead of glycerol and incubated for 48 h.

The culture supernatant was harvested after centrifugation (3000*g*, 277 K, 5 min).

2.2. Enzymatic activity assay

Endoproteolytic activity was measured with 0.02%(*w*/*v*) resorufin-labelled casein as a substrate (Roche Diagnostics) at pH 7.0 in Tris buffer (50 m*M* final concentration) in a total volume of 0.5 ml (Borg-von Zepelin *et al.*, 1998; Reichard *et al.*, 2006). After incubation at 310 K, the undigested substrate in the enzyme–substrate mixture was precipitated using trichloroacetic acid [4%(*v*/*v*) final concentration] and separated from the supernatant by centrifugation. 500 µl 500 m*M* Tris–HCl buffer pH 9.4 was added to the collected supernatant (neutralization step) and the A_{574} of the mixture (1 ml) was measured. For practical purposes, 1 mU of activity was defined as producing an increase in absorbance of 0.001 per minute in a proteolytic assay (1 ml). As indicated below, activation of the proenzyme occurs early during heterologous expression. Since the purified binary complex is already fully active under the experimental conditions used to measure enzymatic activities, no further purification of the enzyme moiety was necessary for activity measurements.

2.3. Protein purification for structural analysis

Large-scale expression of the protein was performed using 2 l flasks in medium containing glycerol as the carbon source for cell growth and adding methanol until the end of induction, at which point the cells were harvested and the supernatant was recovered and cooled to 377 K. The supernatant was then loaded onto an Ni–NTA agarose column (Qiagen, Valencia, California, USA). Elution was performed using a linear gradient from 5 m*M* to 1 *M* imidazole in 35 column volumes in an ÄKTApurifier FPLC system (GE Healthcare, Piscataway, New Jersey, USA). The protein eluted from the Ni–NTA column was then desalted whilst concentrating using a Centricon centrifugal filter device (Millipore, Billerica, Massachusetts, USA) against 20 m*M* Tris pH 7.5. The protein, at a concentration of 28 mg ml^{-1}, was aliquoted and stored for subsequent screening of crystallization conditions.

Attempts were made to obtain non-autoproteolyzed enzyme samples by using protease inhibitors. Invariably, the addition of inhibitor cocktails with and without EDTA either during the induction or purification steps led to the detection of two separate polypeptide chains with different molecular masses on SDS–PAGE: one corresponding to the catalytic domain and a second smeared band corresponding to the prodomain (data not shown). Therefore, it can be deduced that the autoproteolytic activation of the enzyme occurs early during its expression in the host.

2.4. Protein crystallization and preparation of heavy-metal derivatives

A. fumigatus fungalysin was crystallized using the sitting-drop vapour-diffusion method. Initial searches for crystallization conditions were performed in a high-throughput setting using several commercially available kits and incubation in crystal farms at steady temperatures of 277 and 293 K. Among the crystallization conditions tested, the best results were obtained with PEG 1500 as the precipitant and a mixture of organic buffers at a low pH range (pH 4.0 and 5.0). Some crystals that grew from the initial screening tests diffracted to resolutions ranging between 2.4 and 2.0 Å at the ESRF synchrotron (beamline ID14-4). The initial crystallization conditions were optimized such that adequate crystals were obtained for screening of heavy atoms. The best crystals were grown from a 1 µl:1 µl mixture of sample (AfuMep at 14 mg ml^{-1} in 0.02 *M* Tris pH 7.5) and precipitant solution (malonate/imidazole/borate pH 4.0, 20% PEG 1500) using the vapour-diffusion method in 24-well Cryschem plates. Crystals (Supplementary Fig. S1[1]) were manually harvested and transferred to a new drop containing the precipitant solution plus a millimolar amount of each heavy atom tested. To prevent crystal damage, baths in increasing heavy-atom concentrations were performed using different time intervals. For data collection, crystals were harvested, briefly bathed in cryoprotectant buffer (*i.e.* the reservoir solution with added 30% glycerol) and cryocooled; diffraction data were then collected.

2.5. Structure solution and refinement

Given the HE*XX*H sequence motif common to AfuMep and M4 bacterial peptidases, initial attempts at solving the crystal structure were performed using the molecular-replacement method (MR). However, we were unable to obtain a model using the available three-dimensional structures of vibriolysin (PDB entry 3nqy; Gao *et al.*, 2010), elastase (PDB entry 3dbk; M. T. Overgaard &. D. B. McKay, unpublished work), thermolysin (PDB entry 3p7p; D. H. Juers & M. Weik, unpublished work) or fragments of them as search models, likely owing to the low sequence similarity. Phasing was made possible from a K_2PtCl_4-derivatized crystal by using *SHELXD*/*E* (Sheldrick, 2008) for substructure solution, site selection and enantiomorph determination; *SHELXE*/*MLPHARE* (Otwinowski, 1991) for heavy-atom refinement and phase calculation; *DM* (Cowtan, 1994) for density modification; and *RESOLVE*/*Buccaneer* (Terwilliger, 2004; Cowtan, 2006) for model building. To improve the initial model the *MRSAD* procedure within *Auto-Rickshaw* (Panjikar *et al.*, 2005, 2009) was followed. This 3.3 Å resolution structure was used to phase the native data *via* MR in *Phaser* (McCoy *et al.*, 2007). Manual building and readjustments were performed in *Coot* (Emsley *et al.*, 2010). The polypeptide chain could be unambiguously traced from the N-terminal residue 31 of the prodomain to the C-terminal Cys634 of the catalytic domain. However, two loop regions in the prodomain, residues 58–63 and 178–179, are not defined in density and their coordinates were not included in the final model. During early structure refinement a conspicuous electron-density peak not far from the calcium ion was evident. Attempts to refine it as

[1] Supplementary material has been deposited in the IUCr electronic archive (Reference: DW5058). Services for accessing this material are described at the back of the journal.

calcium at full occupancy resulted in significant negative peaks of electron density and high atomic displacement parameters compared with those of neighbouring atoms. Use of a partial occupancy refinement model yielded a reasonable refined structure with an isotropic *B* factor congruent with those of the liganded atoms. Asn47 in the prodomain is glycosylated and the electron density was interpreted as an (*N*-acetylglucosamine)$_2$–mannose chain. Extra electron density corresponding to a molecule bearing two planar carboxylate groups was clearly evident in the region near the catalytic zinc ion and was interpreted as a malonate from the crystallization buffer. Other ligands include borate, also originating from the crystallization buffer, and glycerol, which was used as the cryoprotectant. The refinement progressed to convergence and reached an excellent agreement between the model and the experimental data as shown by the statistics listed in Table 1. Data collections were performed on ESRF beamlines ID14-4 and ID23-1 (McCarthy *et al.*, 2009; Nurizzo *et al.*, 2006). X-ray diffraction data were processed with *XDS* (Kabsch, 2010) and programs from the *CCP*4 suite (Winn *et al.*, 2011). *REFMAC* (Murshudov *et al.*, 2011) was used in different stages of structure refinement. *MolProbity* (Chen *et al.*, 2010) was employed to check the protein coordinates against reference geometric values. *SURFNET* (Laskowski, 1995) was used to analyze the surface of the protein for voids and clefts. Figures were prepared with *ESPript* (Gouet *et al.*, 1999) and *PyMOL* (http://www.pymol.org).

Table 1
Statistics of data collection and refinement for *A. fumigatus* M36 metallopeptidase.

Values in parentheses are for the outer shell.

	AfuMep, native	AfuMep, derivative
Wavelength (Å)	0.97629	1.07183
Space group	$P6_5$ (one molecule per asymmetric unit)	
Unit cell parameters (Å)	$a = b$85.40, c = 176.09	$a = b$85.63, c = 180.74
Resolution range (Å)	21.0–1.80 (1.90–1.80)	30.0–3.30 (3.43–3.30)
No. of measured/unique reflections	482319/67131	106950/11305
$R_{\rm merge}$† (%)	5.7 (41.3)	15.9 (51.9)
Completeness (%)	100.0 (100.0)	
Multiplicity	7.2 (6.7)	
Anomalous completeness (%)		99.9 (99.9)
Anomalous multiplicity		4.8 (4.8)
$\langle I/\sigma(I)\rangle$	22.3 (4.3)	14.3 (4.5)
Refinement statistics		
Reflections used (total/test set)	66342/3395	
Crystallographic *R* factor‡/$R_{\rm free}$§	16.7/19.7	
R.m.s.d. bond lengths (Å)	0.010	
R.m.s.d. bond angles (°)	1.20	
No. of protein atoms/total atoms	4595/5191	
B-factor statistics (Å^2)		
Overall *B* factor/Wilson *B* factor	19.9/23.3	
Catalytic domain (main/side chain)	19.7/20.8	
Prodomain (main/side chain)	24.4/25.1	
Zn^{2+} (1 in total/1 molecule per monomer)	14.8	
Ca^{2+} (2 in total/2 molecules per monomer)	15.2 [Ca1]/19.4 [Ca2]	
Malonate/borate (1 molecule/3 molecules per monomer)	50.8/38.5	
N-Acetylglucosamine/mannose (2 molecules/1 molecule per monomer)	34.0	
Glycerol atoms (3 molecules per monomer)	39.3	
Solvent atoms (520 in total)	37.0	
Protein geometry¶		
Ramachandran favoured (%)	96.1 [565 of 588 residues]	
Ramachandran allowed (%)	99.4 [584 of 588 residues]	
Ramachandran outliers (%)	0.6 [4 of 588 residues]	

† $R_{\rm merge} = \sum_{hkl}\sum_i |I_i(hkl) - \langle I(hkl)\rangle|/\sum_{hkl}\sum_i I_i(hkl)$. ‡ *R* factor $= \sum_{hkl}||F_{\rm obs}| - |F_{\rm calc}||/\sum_{hkl}|F_{\rm obs}|$, where $F_{\rm obs}$ and $F_{\rm calc}$ are the observed and calculated structure-factor amplitudes of reflection *hkl*. § $R_{\rm free}$ is equal to *R* factor for a randomly selected 5.0% subset of the total reflections that were held aside throughout refinement for cross-validation. ¶ According to *MolProbity* (Chen *et al.*, 2010).

2.6. Circular-dichroism analysis

Circular-dichroism (CD) spectra in the far-UV and near-UV regions were obtained using a Jasco 715 spectropolarimeter equipped with a thermostat-controlled cell holder. Scans were conducted between 298 and 368 K at a scan rate of 0.5 K min^{-1}. For AfuMep changes in the CD signal at 210 nm were recorded at a cell path length of 0.2 cm and a protein concentration of 5 µ*M* in 10 m*M* sodium phosphate buffer pH 7.0. Thermolysin measurements were recorded at 217 nm at a cell path length of 0.2 cm with a protein concentration of 10 µ*M* in 10 m*M* sodium phosphate buffer pH 7.0. Elastase changes in the CD signal were recorded in the near-UV region at 280 nm with a cell path length of 1 cm and a protein concentration of 70 µ*M* in 10 m*M* sodium phosphate buffer pH 7.0. Thermolysin and elastase were purchased from Sigma.

2.7. Western blot analysis

5 µl of *P. pastoris* culture supernatant was loaded per lane on a 12% SDS–PAGE gel. An antiserum was made in a rabbit using purified AfuMep as an antigen. Western blots were revealed using the prepared rabbit antiserum and alkaline phosphatase-conjugated goat antirabbit IgG (Bio-Rad, Hercules, California, USA).

3. Results and discussion

3.1. Crystallization and structure solution

The 1.8 Å resolution refined AfuMep crystallized in the hexagonal space group $P6_5$ with one molecule per asymmetric unit consisting of two separate polypeptide chains: the catalytic domain (residues 246–634) harbouring the catalytic zinc ion and the cleaved propeptide (residues 31–245). Additional molecular ligands include glycerol, which was used as the

cryoprotectant, and malonate/borate, which was possibly incorporated from the mother liquor. The structure was refined with excellent agreement with the diffraction data to an R factor of 16.7% and an R_{free} of 19.7%. Further crystallographic and refinement statistics are presented in Table 1. The atomic coordinates and structure factors have been validated and deposited with the PDB under accession code 4k90.

3.2. The structure of the prodomain

Residues 19–245 of the proAfuMep sequence correspond to the prodomain region. No electron density was detected for residues 19–30, 58–63 and 178–179, which are located in solvent-exposed loops, an observation that is probably related to the flexibility of these regions. Two similar subdomains sitting over opposite faces of the catalytic domain can be easily distinguished (Figs. 1*a* and 1*b*). A peptide linker consisting of the short α-helix 3 connects the subdomains which are made up of a four-turn α-helix packed against a five-stranded antiparallel β-sheet (α-helix 2 and β-strands 2–6 in the N-terminal subdomain, and α-helix 4 and β-strands 7–11 in the C-terminal subdomain). Each single subdomain has its β-sheet concave surface packed against the catalytic domain, while its outward-looking α-helix convex surface is exposed to the external milieu.

The AfuMep prodomain bears some similarity to known protein folds. Searches of all available tertiary structures in the PDB with the *DALI* server (Holm & Rosenström, 2010) revealed that the highest scorers were vibriolysin prodomain (PDB entry 3nqy; Z-score 11.8; 14% sequence identity; r.m.s.d. of 2.6 Å over 140 aligned C^{α} atoms; Gao *et al.*, 2010) and YycI, a membrane-anchored protein from *Bacillus subtilis* (PDB entry 2o3o; Z-score 8.2 over 136 C^{α} atoms; Santelli *et al.*,

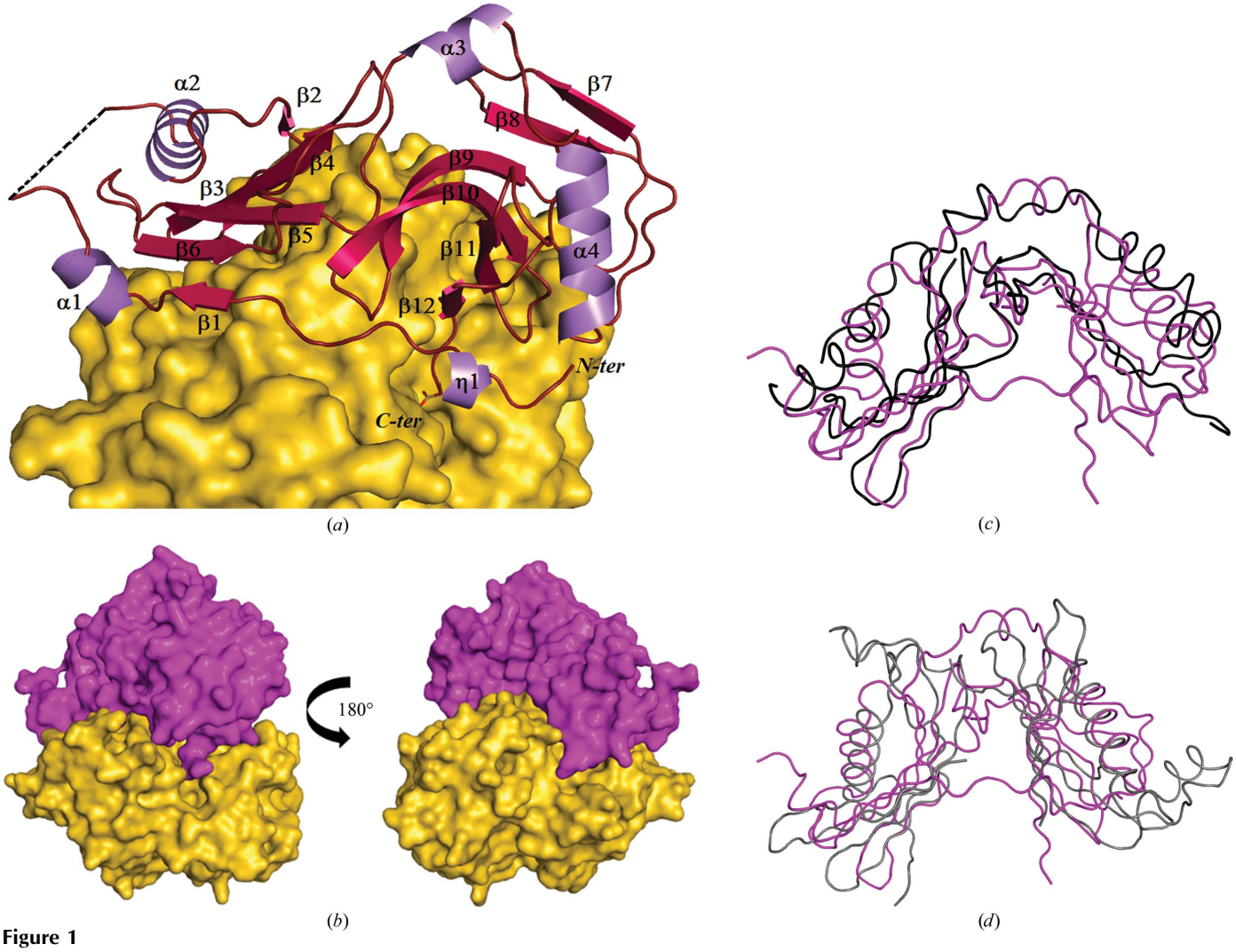

Figure 1
(*a*) The prodomain is shown as a cartoon with secondary-structure elements coloured in tones of violet. The secondary-structure elements are coloured violet (α-helices), dark red (β-sheets) and brown (loops) and are labelled. Broken lines indicate residues 58–63 that were not seen in the electron density. The C-terminal Glu245 is shown as sticks. The catalytic domain is shown as an opaque surface in gold. (*b*) View of the prodomain (surface in violet) in complex with the catalytic domain (gold). Left panel, same orientation as in (*a*); right panel, view rotated by 180°. (*c*) AfuMep propeptide (backbone trace in violet) superimposed on the vibriolysin FTP domain (black). (*d*) Two molecules of chicken egg-white cystatin (PDB entry 1cew; grey), superimposed onto regions 31–140 and 141–245 of AfuMep propeptide. The orientation is the same as in (*c*).

2007). The vibriolysin prodomain is composed of two distinct globular subdomains called PepSY ('peptidase propeptide and YpeB domain') and FTP ('fungalysin–thermolysin propeptide'), which were first identified from sequence-database searches (Yeats *et al.*, 2004). According to this, bacterial vibriolysin and fungalysin share one FTP domain but not the PepSY domain, which is lacking in the latter. Fig. 1(*c*) shows the superimposition of vibriolysin and fungalysin prodomains.

A close inspection revealed that each subdomain in the AfuMep prodomain is strikingly similar to members of the cystatin superfamily, particularly to a large group of protease inhibitors called cystatins, although with a lower score. Cystatins specifically inhibit cysteine proteases such as plant papain and mammalian cathepsins (Benchabane *et al.*, 2010). A superimposition of chicken egg-white cystatin (PDB entry 1cew; *Z*-score of 4.7 over 66 aligned C^{α} atoms; Bode *et al.*, 1988) indicates that two copies of the fold exist in the AfuMep prodomain (Fig. 1*d*). This feature is shared by human latexin, alias endogenous carboxypeptidase inhibitor (PDB entry 2bo9; *Z*-score of 3.7 over 76 aligned C^{α} atoms; Pallarès *et al.*, 2005), a specific inhibitor of metallopeptidases of the M14 family, yet the orientation of the cystatin subunits in latexin is reversed, *i.e.* the α-helices face the catalytic unit in the CPA4–latexin complex (Pallarès *et al.*, 2005). Thus, this is the first report of a fungalysin prodomain tertiary structure which can also be described as a new fold.

3.3. The prodomain–catalytic domain interface

The accessible surface areas for the isolated prodomain and catalytic domain structures span 11 435 and 14 150 Å^2, respectively. The interface with the catalytic domain extends to about 2000 Å^2 as the prodomain contacts the catalytic domain β-strands 17 and 18 as well as α-helices 6, 7 and 9–11 (Fig. 2 and Supplementary Table S1).

The C-terminus of the prodomain is settled along the nonprimed subsites (residues located N-terminally from the scissile peptide bond) of the active-site pocket of the catalytic domain. The α-carboxylic acid of the C-terminal Glu245 coordinates the zinc monodentately, indicating that the catalytic cleavage reaction had taken place abrogating the Glu245-Ala246 scissile amide bond. The liberated Ala246 is clearly seen in the electron-density maps, yet the primed subsites (residues located C-terminally from the scissile peptide bond) in the active-site cleft are unoccupied owing to a large conformational change of the newly created N-terminus (as will be discussed below).

3.4. The overall structure of the catalytic domain and its affiliation to known folds

The catalytic domain has an overall oval shape with approximate dimensions of 30 Å in width by 60 Å in length and with a long depression or cleft that harbours the catalytic zinc ion. This depression runs more or less along the interface between α-helices 6 and 7, which are the boundaries of two distinct subdomains: the α/β N-terminal subdomain and the primarily α-helical C-terminal subdomain (Fig. 3*a*). The cleft has its longest axis of about 32 Å limited by Asn447 (in the turn connecting α-helices 6 and 7) and Arg490 (close to α-helix 8), with its narrowest dimension of about 6 Å being defined by Asn392 (between β16/17) and His520 (α-helix 9) in the vicinity of the catalytic zinc site (Fig. 3*b*). All but one of the four protein ligands that form the zinc coordination sphere are contributed by the catalytic domain, namely His429, His433 and Glu459, with one ligand from the prodomain, *i.e.* Glu245 (Supplementary Table S2). The geometry around the zinc ion is tetrahedral (Fig. 3*c*). With the aim of obtaining the full-length unproteolyzed inactive form of the protein for further studies, we produced site-directed mutants of two zinc ligands, His429Met and Glu459Met, and the catalytically key residue in the HE*XX*H motif, Glu430Ala. Crucially, the protein-expression level of the His429Met and Glu430Ala mutants was not detectable, whereas Glu459Met presented a very low expression level compared with the wild-type protein and with a high degree of partial degradation. Thus, the zinc ion proved to be essential for correct AfuMep expression and folding.

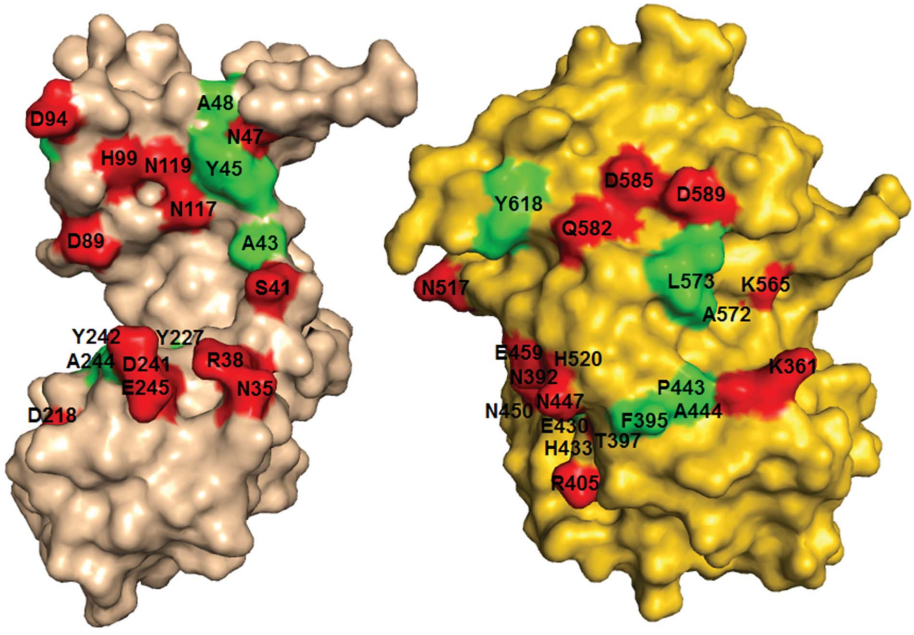

Figure 2
The prodomain (opaque surface in wheat) was hinge-moved to show major hydrogen-bonding contacts with the catalytic domain (gold). Key residues are coloured (red, polar side chains; green, nonpolar side chains) and labelled. Residues shown are in accordance with Supplementary Table S2.

The overall tertiary structure of the AfuMep catalytic domain is reminiscent of the bacterial peptidases of the thermolysin family in spite of low

sequence homology (see Supplementary Fig. S2). Consequently, we went on to establish its underlying features *via* further biochemical and functional studies, as will be discussed in the closing sections of this paper.

3.5. The C-terminal disulfide bridge in the fungalysin catalytic domain

The first of the two disulfide bridges in the catalytic domain (Cys448–Cys576) links α-helices 7 and 11 and lies in the core of the catalytic domain close to the metal centres, whereas the second disulfide bridge (Cys601–Cys634) joins the C-terminus to α-helix 12, which is located externally and is fully exposed to the solvent (Fig. 4*a*). An inspection of the primary structure of M36 peptidases shows a conserved C-terminal cysteine separated from a second cysteine by about 30 residues internally, suggesting that the C-terminal disulfide bridge could be important for structural stability. Bacterial elastase has a C-terminal disulfide bridge which has been shown to have a critical role in the enzymatic activity (Ogino *et al.*, 2001). In the native crystal structure the C-terminus of the protein is primarily stabilized by the packing of hydrophobic side chains in such a way that the C-terminal Cys601–Cys634 disulfide bond and the surrounding secondary-structure elements are clearly seen in the electron-density maps. In the Pt-derivative crystal structure this disulfide bond is cleaved (Fig. 4*b*), leading to disorder such that residues at the C-terminus are undetected in the electron-density maps.

A Cys634Ala single-point mutant produced to further investigate the properties of the C-terminal cysteine is poorly expressed compared with the wild-type enzyme, indicating a possible structural impairment. Probably owing to the fact that Cys634 is far from the active site, the mutant still displays catalytic activity against the substrate casein (data not shown).

3.6. Arg470: a positively charged side chain in place of calcium

A network of water molecules delineates a path that runs from the catalytic zinc ion to the opposite surface of the protein. This 12 Å long channel is mostly lined by hydrophilic side chains such as (listed from the nearest to the farthest with respect to the zinc): Asp463, Arg495, Met483, Thr467, Arg470, Asn256, Glu260, Glu423, Asp257, Thr259 and Thr482 (Figs. 5*a* and 5*b*). Met483 and Gly484 in the loop between α-helices 7 and 8 seem to constrain the distal part of this channel. Water

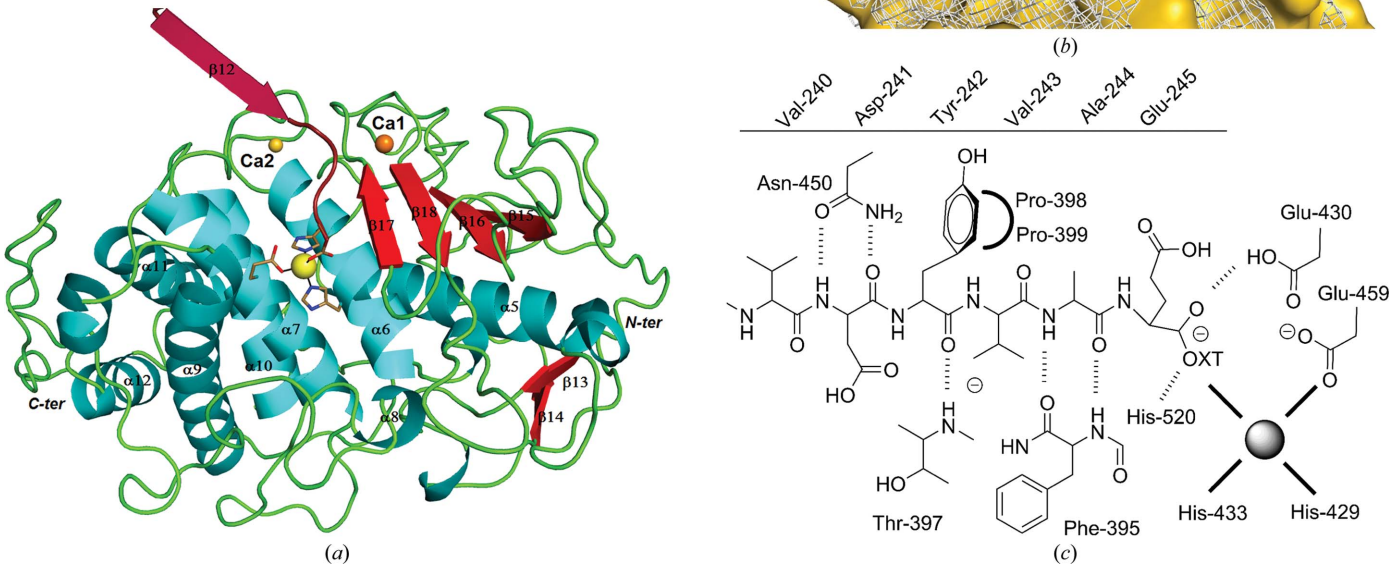

Figure 3
(*a*) The catalytic domain is represented as a cartoon with secondary-structure elements coloured cyan (α-helices), red (β-sheets) and green (loops) and labelled according to the sequence. The catalytic zinc is shown as a sphere (yellow) with its ligands as sticks (N atoms coloured blue, O atoms red and C atoms pale brown). β-Strand 12 from the propeptide (partly shown for clarity) is in dark red, with its C-terminal residue, Glu245, shown as sticks. Two calcium ions are depicted in tones of orange. (*b*) Detail of the active-site cleft of the catalytic domain (surface in gold). The C-terminal residues from the prodomain Tyr242-Val243-Ala244-Glu245 are shown as sticks. Important residues are labelled (see text) and the major void in the structure is shown as a wire mesh in white. Voids were retrieved with *SURFNET* (Laskowski, 1995). (*c*) Schematic depiction of (*b*). The six C-terminal residues of the propeptide (named at the top of the figure) are shown with catalytic domain residues (labelled). Hydrogen-bond interactions are shown as dashed lines, while the Zn^{2+} coordination sphere is shown as a continuous bold line.

molecules providing a multitude of hydrogen-bond interactions are predominately found around Arg470.

Surprisingly, the location of the guanidinium side chain of Arg470 corresponds to that of the Ca^{2+} ion in elastase and thermolysin (Figs. 6*a* and 6*b*). Furthermore, the distance from Arg470 to the catalytic zinc ion equals the Zn–Ca separation in these enzymes (about 16 Å). Although α-helix 7 in AfuMep has a structural counterpart in elastase and thermolysin, that in the bacterial peptidases is extended by two additional turns, contains one calcium ligand and continues through a short loop that harbours two further metal-ion ligands. Thus, three potential metal-ion ligands are absent in AfuMep. It is worth mentioning that in thermolysin the calcium ions have no catalytic activity but rather may play a role in stabilizing the enzyme against autolysis (van den Burg & Eijsink, 2004). In addition, Lys197 in the thermolysin-like protealysin is thought to compensate for the lack of calcium in the crystal structure (Demidyuk *et al.*, 2010).

Given its similarity to calcium in bacterial proteases and its invariance among fungalysins, we further investigated the possible functional role of Arg470 by designing a series of variants, namely Arg470Ala, Arg470Glu, Arg470Ser and Arg470Lys. It was promptly established that the secretion levels of these mutants were dramatically affected, depending on the nature of the side chain involved, when compared with the secretion levels of the wild-type enzyme (Fig. 6*c*). This was so much so that for the negatively charged side chain Arg470Glu the level of secretion was virtually nonexistent, whilst for the smaller noncharged side chains Arg470Ser and Arg470Ala it was somewhat increased. The change from a

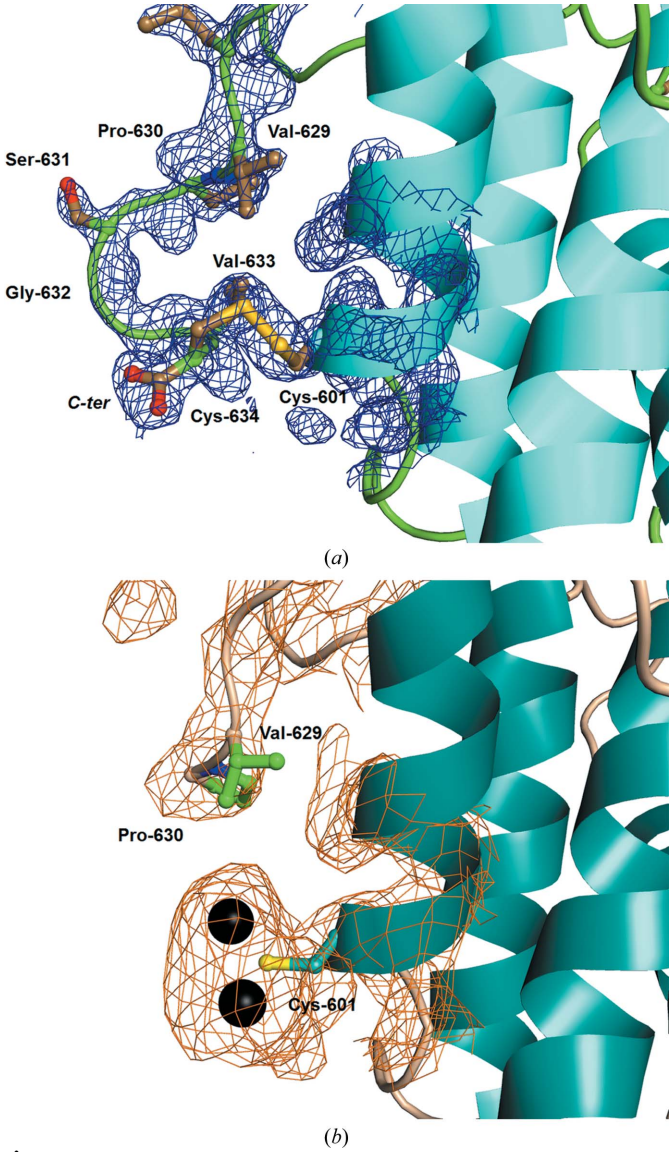

Figure 4
(*a*) The C-terminus of AfuMep, Val629-Pro630-Ser631-Gly632-Val633-Cys634, is shown as sticks and labelled. Also shown are the α-carboxylate from Cys634 and the Cys601–Cys634 disulfide bridge with the S—S bond in yellow. The electron-density map is contoured at a 1.0σ level (blue mesh). (*b*) In the platinum derivative, electron density allowed the modelling of Val629-Pro630 (shown as sticks in green) beyond which the electron density is very weak. The Cys601–Cys634 disulfide bridge is cleaved while Cys601 is covalently bound to two Pt ions (spheres in black).

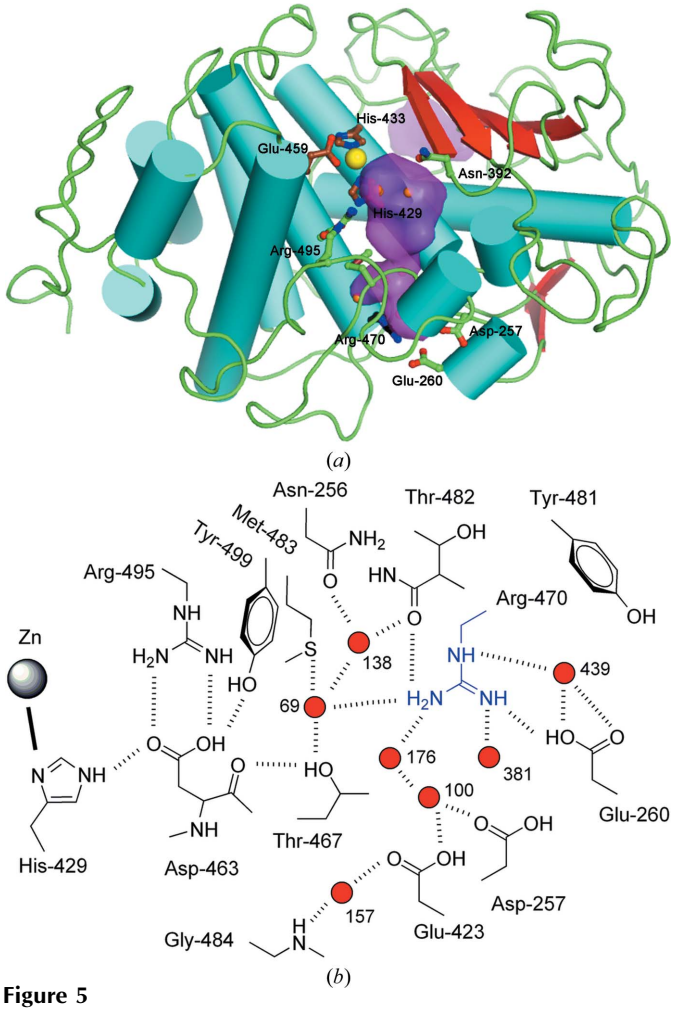

Figure 5
(*a*) Cartoon representation of the catalytic domain showing the largest cavity in AfuMep (surface in magenta). The zinc is depicted as a sphere in yellow and important residues are shown as sticks. Water molecules are shown as spheres. (*b*) Schematic representation of the Arg470 ionic environment. Key residues as well as water molecules (filled circles in red) are shown and labelled. The Arg470 side chain is coloured blue. The catalytic Zn^{2+} ion (far left, depicted as a sphere) is also shown.

positively charged arginine to a lysine (Arg470Lys) was least detrimental to the secretion level. The specific activity of the mutated Meps remained the same as the non-mutated enzyme (data not shown). It can be concluded from the structural comparisons and from the single mutants produced that the role of Arg470 is important for the proper folding and catalytic activity of the enzyme, as is calcium in bacterial M4 metallopeptidases.

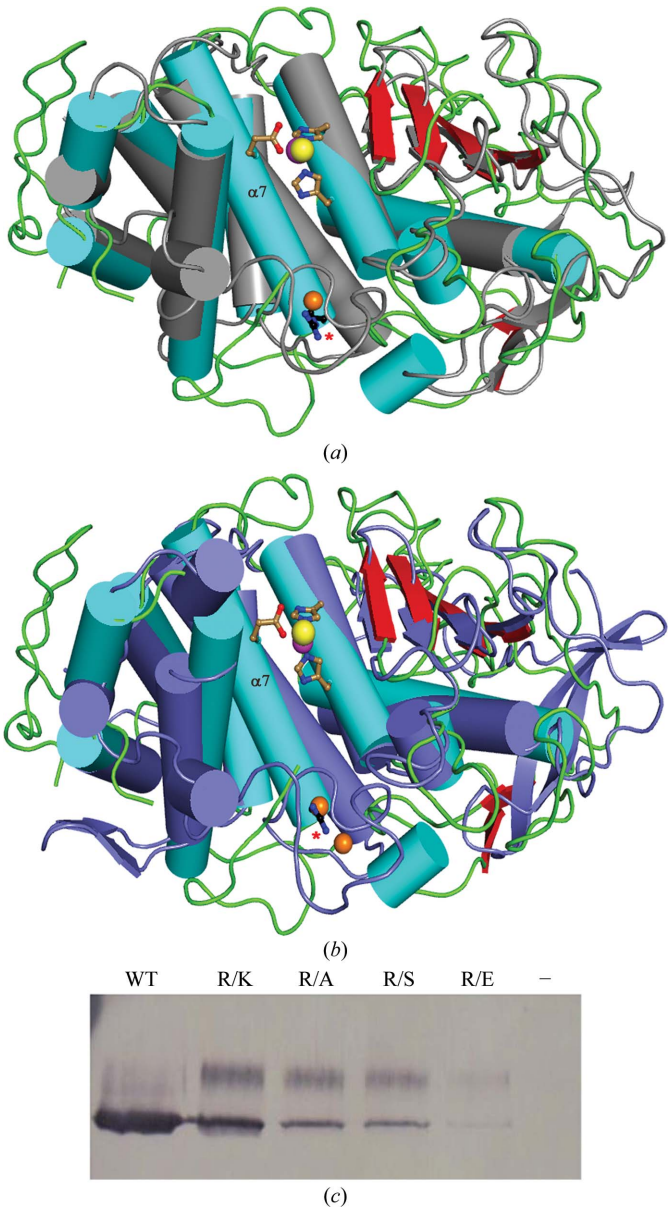

Figure 6
(*a*) The AfuMep catalytic domain structure superimposed with elastase (grey). Arg470, His429, His433 and Glu459 are shown as sticks (Arg470 C atoms are shown in black and its location is indicated by an asterisk). For elastase, zinc and calcium are shown as violet and orange spheres, respectively. α-Helix 8 and surrounding loops in AfuMep covering Arg470 are omitted for clarity. (*b*) The same as (*a*) but with thermolysin (blue) instead of elastase. (*c*) Western blot of recombinant *A. fumigatus* wild-type and mutated AfuMep in *P. pastoris* culture supernatant. WT indicated nonmutated AfuMep. R/K, R/A, R/S and R/E indicate Arg470Lys, Arg470Ala, Arg470Ser and Arg470Glu mutated AfuMep, respectively. The upper band corresponds to the full-length proenzyme and the lower band corresponds to the catalytic domain. – indicates the supernatant of *P. pastoris* GS115 which does not express any AfuMep.

3.7. Calcium and structural stability in fungalysin

The fungalysin structure harbours two calcium metal ions that are mutually separated by 11 Å and are at distances of 16 and 20 Å from the zinc, respectively. The most striking feature is their lack of a relationship to those in elastase and thermolysin. Structural superimposition indicates that the calciums in AfuMep are bound in completely different locations compared with those found in the bacterial peptidases. Conversely, the metal ion in the bacterial peptidases matches no bound metal ions in the AfuMep structure but rather the Arg470 guanidinium side chain (see §3.6 and Fig. 6).

To investigate whether the observed structural differences would have any effect on protein stability, the thermal unfolding processes of AfuMep, elastase and thermolysin were compared (Fig. 7). In the far-UV domain, where the CD signal was monitored at 210 nm for AfuMep and at 217 nm for thermolysin, a single-step transition was observed with a midpoint temperature of 326 K for AfuMep and 345 K for thermolysin. In the far-UV domain, the CD spectra of elastase at 298 K was not significantly different from that obtained at 368 K, as has been reported by others (Bousquet *et al.*, 2003). Therefore, to allow greater precision, the denaturing curve of elastase was obtained in the near-UV domain by monitoring the CD signal at 280 nm, where two transitions can be distinguished at midpoint temperatures of 325 and 348 K. This suggests a sequential unfolding process and that the tertiary structure of elastase is more sensitive than its secondary structure to thermal denaturation. This is in agreement with previous results, where the temperature required for half-maximal inactivation of porcine elastase was found to be 336 K (Asgeirsson *et al.*, 1993). Differences at the primary-sequence level leading either to the creation of binding sites for exogenous calcium (elastase, thermolysin) or the establishment of an endogenous positively charged side chain (Arg470 in AfuMep) may be important factors in the different stabilities observed for these enzymes.

3.8. Remodelling of the N-terminus of the catalytic domain

Proteolytic cleavage at the Glu245–Ala246 junction generates two novel polypeptide chains: the prodomain, with its newly created C-terminal Glu245, and the catalytic domain, which now has Ala246 as the N-terminus. While the Glu245 C-terminus of the prodomain remains bound to the non-primed sites in the active-site pocket of the enzyme, the second product of the reaction, the polypeptide with N-terminal Ala246, is liberated and leaves the primed sites unoccupied. Modelling of the non-autoproteolyzed enzyme shows that the stretch of 12 residues beyond Ala246 ('sequence 246–258'; Fig. 8, loop in black) would be placed to allow the 245–246 amide bond to undergo catalytic attack (Fig. 8, arrow). Once this has occurred, sequence 246–258 would be displaced to near the position of β-strand 14 in order to repack against it and the Ser/Pro-rich region in the long

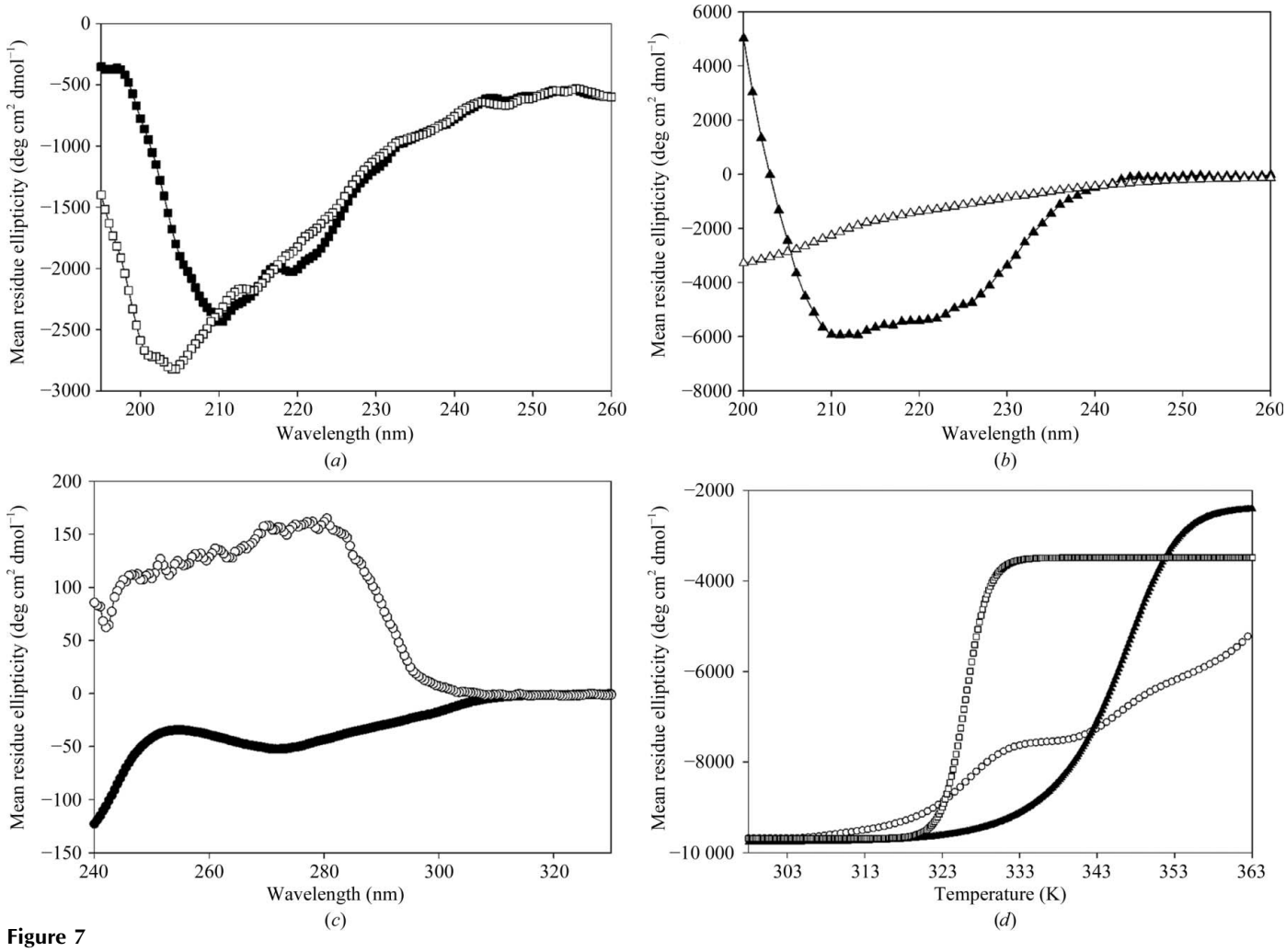

Figure 7
Thermal stability monitored by circular dichroism. (*a*) AfuMep far-UV circular-dichroism spectra measured at 298 K (filled squares) and 368 K (squares). (*b*) Thermolysin far-UV circular-dichroism spectra measured at 298 K (filled triangles) and 368 K (triangles). (*c*) Elastase near-UV circular-dichroism spectra measured at 298 K (filled circles) and 368 K (circles). (*d*) Temperature-induced ellipticity changes of AfuMep at 210 nm (squares), thermolysin at 217 nm (filled triangles) and elastase at 280 nm (circles).

loop between β-strand 15 and α-helix 5. A large conformational change consisting of a 30 Å sweep would be necessary to ensure correct positioning of the fragment in its final location in the mature enzyme (Fig. 8, to the right) forming β-strand 13. The 3_{10}-helix located between β-strands 13 and 14 containing the invariant Pro258 may act as the hinge that facilitates the shift of the polypeptide chain towards its mature conformation. It is worth mentioning that the N-terminal region of AfuMep, which is mostly a long loop with short intervening β-strands 14–15, may provide an adequate flexible environment to accommodate the mobile new β-strand 13 once the cleavage of the propeptide–catalytic domain bond has taken place. Flexibility can be estimated by observing that the average main-chain *B* factor for residues 246–333 is 25.4 (0.4) Å^2, which is markedly higher compared with the overall value of 19.7 (0.4) Å^2. Such a rearrangement of the N-terminal end of the catalytic domain seems to conform to the autoprocessing and energy-driven conformational change model proposed previously for maturation of the thermolysin-like peptidase vibriolysin (Gao *et al.*, 2010). According to this model, maturation of the zymogen begins with an autoproteolytic cleavage of the bond between the catalytic domain and the prodomain, followed by an energy-driven rearrangement of the newly created N-terminal end of the catalytic domain. The cleaved propeptide remains bound to the catalytic domain in a metastable state, which progresses to final maturation through stepwise degradation of the prodomain and release of the mature enzyme. This would be the case for AfuMep prodomain, the structure of which appears to be N-terminally truncated and with other internal positions that are not observed in the electron-density maps, as is the case for the loop between α-helices 1 and 2 coincident with a proteolyzed region in the vibriolysin prodomain.

4. Conclusions

The X-ray crystallographic analysis of the *A. fumigatus* secreted fungalysin Mep at a resolution of 1.8 Å represents the first structural determination of a protease of the M36 family. The three-dimensional structure consists of the complex

formed by the prodomain and the full-length catalytic domain. The prodomain, cleaved from the catalytic domain, has a hinge-shaped bilobal arrangement composed of a pair of cystatin fold-like globular subdomains and contains regions where the absence of electron density may be interpreted as intrinsic flexibility. Furthermore, structural remodelling of the N-terminal end of the catalytic domain seems to follow a maturation pattern recently proposed by other authors corresponding to a large conformational change followed by refolding and accommodation into a new position in the structure. Thus, the structure presented here may be regarded as a complex in which the prodomain and catalytic domain are separated polypeptide chains forming a binary assembly in which the prodomain is being reshaped by the catalytic domain. This dynamic behaviour in the complex is in agreement with our observations that the polypeptide is fully active when recombinantly expressed and secreted into the supernatant of the *P. pastoris* culture medium.

Structure determination at high resolution allowed a deeper understanding of the properties of the AfuMep catalytic domain. Although the AfuMep crystal structure contains calcium, as do the bacterial M4 peptidases elastase and thermolysin, its location differs completely owing to local structural variations. AfuMep is also distinctly thermally unstable compared with elastase and thermolysin. Calcium in the latter peptidases is replaced by a guanidinium side chain in fungalysin, Arg470. It also acts as a link for the catalytic zinc to the external milieu, sustaining a water-filled path. Single-point mutations of this amino-acid position and structural evidence point to a key role in protein function as for calcium in bacterial peptidases. The conservation of Arg470 among the fungalysin family members might point to a distinctive evolutionary trait. Fungalysin possesses a pair of disulfide bridges that are present in almost all members of the M36 family of fungalysins. One of them is located C-terminally and consists of the last cysteine residue in the genomic sequence (Cys634). This residue forms a disulfide bond to Cys601, bridging the C-terminus to α-helix 12. Abrogation of this disulfide bridge may affect the structural stability of the protein since a Cys634Ala mutant is poorly expressed and the C-terminal region appears to be disordered and displays the internal cysteine covalently bound to platinum as a thiol group in the heavy-atom derivative crystals.

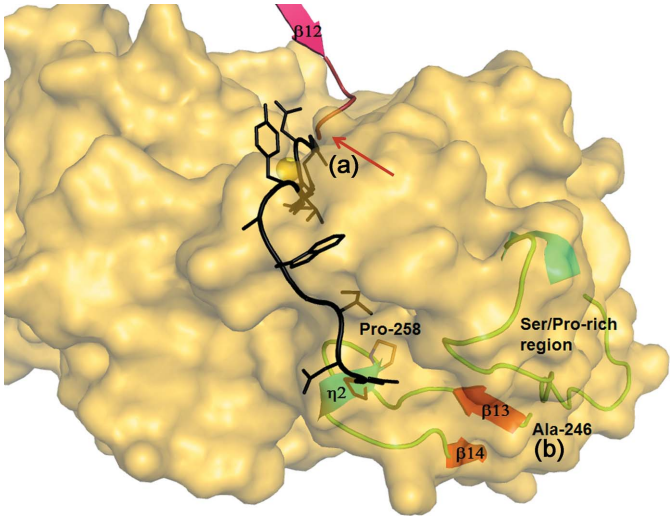

Figure 8
The catalytic domain is represented as a translucent surface in gold. The catalytic zinc is shown as a sphere (yellow), β-sheet 12 from the propeptide is shown in dark red and the peptide bond between the C-terminal residue of the prodomain and the first residue in the enzyme is indicated by a thin red arrow. In the uncleaved state, sequence 246–258 (loop in black) would occupy the catalytic site cleft, with Ala246 (the N-terminus of the enzyme) close to the catalytic zinc (position a). Once the mature enzyme state is achieved, sequence 246–258 would pivot on the 3_{10}-helix (η2) close to Pro258 to occupy a new position between β-sheet 14 and the Ser/Pro-rich region to shape the new N-terminal β-sheet 13 in the catalytic domain (position b).

A total of 46 genes encoding putative secreted proteases from 14 different families have been recorded for the *A. fumigatus* genome. The distribution of members of several families such as pepsins (A1 family) is widespread among kingdoms. In contrast, the M36 family is a typical fungal family (Monod *et al.*, 2009). The *A. fumigatus* genome encodes only AfuMep as an M36 protease, but specialized pathogenic fungi such as dermatophytes were found to secrete multiple metallopeptidases of the fungalysin family, *i.e.* Mep1–Mep5 (Monod, 2008). The emergence of multigenic families is most frequently owing to ancient gene-duplication processes that allow organisms to better adapt to different environmental conditions and represent a virulence trend. Mature fungal secreted proteases serve the important functions of breaking down proteinaceous material, splitting large peptides into assailable material for nutrition and for colonization and evading the immune system of the host (Behnsen *et al.*, 2010; Monod *et al.*, 2009). Such key features for the biology and pathology of fungi make secreted proteases potential candidates for therapeutic intervention (Monod *et al.*, 2010; Yike, 2011). The impact of structural knowledge on the discovery of drugs targeting proteases from different classes and the availability of benchmark metallopeptidases such as thermolysin in identifying and characterizing new generations of molecules (Castro *et al.*, 2011; Cudic & Fields, 2009; Deu *et al.*, 2012; Englert *et al.*, 2010; Fernández *et al.*, 2010; Mittl & Grütter, 2006) have been recognized on numerous occasions. Likewise, the newly described fungalysin crystal structure should open the way for further biomedical prospective investigations in the search for better antifungals or diagnostic tools for pathogenic fungi.

We thank Dr Salyha Ali (ESRF) for thorough proofreading of the manuscript and Karine Salamin for her technical expertise in the construction of AfuMep mutants. This work was supported by Ministerio de Economía y Competitividad, Spain (grants BIO2010-22321-C02-01 and BIO2010-22321-C02-02) and Generalitat de Catalunya (grant 2009 SGR218 and XRB, Xarxa de Referència en Biotecnologia). Part of this work was funded by the European Community's Seventh Framework Programme (FP7/2007-2013) under grant agreement No. 227764 (P-CUBE).

References

Abad, A., Fernández-Molina, J. V., Bikandi, J., Ramírez, A., Margareto, J., Sendino, J., Hernando, F. L., Pontón, J., Garaizar, J. & Rementeria, A. (2010). *Rev. Iberoam. Micol.* **27**, 155–182.

Asgeirsson, B. & Bjarnason, J. B. (1993). *Biochim. Biophys. Acta*, **1164**, 91–100.

Beggah, S., Léchenne, B., Reichard, U., Foundling, S. & Monod, M. (2000). *Microbiology*, **146**, 2765–2773.

Behnsen, J., Lessing, F., Schindler, S., Wartenberg, D., Jacobsen, I. D., Thoen, M., Zipfel, P. F. & Brakhage, A. A. (2010). *Infect. Immun.* **78**, 3585–3594.

Benchabane, M., Schlüter, U., Vorster, J., Goulet, M. C. & Michaud, D. (2010). *Biochimie*, **92**, 1657–1666.

Bode, W., Engh, R., Musil, D., Thiele, U., Huber, R., Karshikov, A., Brzin, J., Kos, J. & Turk, V. (1988). *EMBO J.* **7**, 2593–2599.

Borg-von Zepelin, M., Beggah, S., Boggian, K., Sanglard, D. & Monod, M. (1998). *Mol. Microbiol.* **28**, 543–554.

Bousquet, J.-A., Duranton, J., Mély, Y. & Bieth, J. G. (2003). *Biochem. J.* **370**, 345–349.

Burg, B. van den & Eijsink, V. (2004). *Handbook of Proteolytic Enzymes*, edited by A. J. Barrett, N. D. Rawlings & J. F. Woessner, pp. 375–387. London: Elsevier.

Burmester, A. *et al.* (2011). *Genome Biol.* **12**, R7.

Castro, H. C., Abreu, P. A., Geraldo, R. B., Martins, R. C., dos Santos, R., Loureiro, N. I., Cabral, L. M. & Rodrigues, C. R. (2011). *J. Mol. Recognit.* **24**, 165–181.

Chen, V. B., Arendall, W. B., Headd, J. J., Keedy, D. A., Immormino, R. M., Kapral, G. J., Murray, L. W., Richardson, J. S. & Richardson, D. C. (2010). *Acta Cryst.* D**66**, 12–21.

Cowtan, K. (1994). *Jnt CCP4/ESF–EACBM Newsl. Protein Crystallogr.* **31**, 34–38.

Cowtan, K. (2006). *Acta Cryst.* D**62**, 1002–1011.

Cudic, M. & Fields, G. B. (2009). *Curr. Protein Pept. Sci.* **10**, 297–307.

Dagenais, T. R. & Keller, N. P. (2009). *Clin. Microbiol. Rev.* **22**, 447–465.

Demidyuk, I. V., Gromova, T. Y., Polyakov, K. M., Melik-Adamyan, W. R., Kuranova, I. P. & Kostrov, S. V. (2010). *J. Biol. Chem.* **285**, 2003–2013.

Deu, E., Verdoes, M. & Bogyo, M. (2012). *Nature Struct. Mol. Biol.* **19**, 9–16.

Emsley, P., Lohkamp, B., Scott, W. G. & Cowtan, K. (2010). *Acta Cryst.* D**66**, 486–501.

Englert, L., Silber, K., Steuber, H., Brass, S., Over, B., Gerber, H. D., Heine, A., Diederich, W. E. & Klebe, G. (2010). *ChemMedChem*, **5**, 930–940.

Fernández, D., Pallarès, I., Vendrell, J. & Avilés, F. X. (2010). *Biochimie*, **92**, 1484–1500.

Gao, X., Wang, J., Yu, D.-Q., Bian, F., Xie, B.-B., Chen, X.-L., Zhou, B.-C., Lai, L.-H., Wang, Z.-X., Wu, J.-W. & Zhang, Y.-Z. (2010). *Proc. Natl Acad. Sci. USA*, **107**, 17569–17574.

Gouet, P., Courcelle, E., Stuart, D. I. & Métoz, F. (1999). *Bioinformatics*, **15**, 305–308.

Hohl, T. M. & Feldmesser, M. (2007). *Eukaryot. Cell*, **6**, 1953–1963.

Holm, L. & Rosenström, P. (2010). *Nucleic Acids Res.* **38**, W545–W549.

Jaton-Ogay, K., Paris, S., Huerre, M., Quadroni, M., Falchetto, R., Togni, G., Latgé, J.-P. & Monod, M. (1994). *Mol. Microbiol.* **14**, 917–928.

Jousson, O., Léchenne, B., Bontems, O., Capoccia, S., Mignon, B., Barblan, J., Quadroni, M. & Monod, M. (2004). *Microbiology*, **150**, 301–310.

Kabsch, W. (2010). *Acta Cryst.* D**66**, 125–132.

Laskowski, R. A. (1995). *J. Mol. Graph.* **13**, 323–330.

Latgé, J.-P. (1999). *Clin. Microbiol. Rev.* **12**, 310–350.

McCarthy, A. A., Brockhauser, S., Nurizzo, D., Theveneau, P., Mairs, T., Spruce, D., Guijarro, M., Lesourd, M., Ravelli, R. B. G. & McSweeney, S. (2009). *J. Synchrotron Rad.* **16**, 803–812.

McCormick, A., Loeffler, J. & Ebel, F. (2010). *Cell. Microbiol.* **12**, 1535–1543.

McCoy, A. J., Grosse-Kunstleve, R. W., Adams, P. D., Winn, M. D., Storoni, L. C. & Read, R. J. (2007). *J. Appl. Cryst.* **40**, 658–674.

Markaryan, A., Lee, J. D., Sirakova, T. D. & Kolattukudy, P. E. (1996). *J. Bacteriol.* **178**, 2211–2215.

Markaryan, A., Morozova, I., Yu, H. & Kolattukudy, P. E. (1994). *Infect. Immun.* **62**, 2149–2157.

Mittl, P. R. & Grütter, M. G. (2006). *Curr. Opin. Struct. Biol.* **16**, 769–775.

Monod, M. (2008). *Mycopathologia*, **166**, 285–294.

Monod, M., Jaton-Ogay, K. & Reichard, U. (1999). *Contrib. Microbiol.* **2**, 182–192.

Monod, M., Jousson, O. & Reichard, U. (2009). *Aspergillus fumigatus and Aspergillosis*, edited by J.-P. Latgé & W. J. Steinbach, pp. 87–106. Washington: ASM Press.

Monod, M., Paris, S., Sanglard, D., Jaton-Ogay, K., Bille, J. & Latgé, J.-P. (1993). *Infect. Immun.* **61**, 4099–4104.

Monod, M., Paris, S., Sarfati, J., Jaton-Ogay, K., Ave, P. & Latgé, J.-P. (1993). *FEMS Microbiol. Lett.* **106**, 39–46.

Monod, M., Staib, P., Reichard, U. & Jousson, O. (2010). *Aspartic Acid Proteases as Therapeutic Targets*, edited by A. K. Ghosh, pp. 573–606. Weinheim: Wiley-VCH.

Monod, M., Togni, G., Rahalison, L. & Frenk, E. (1991). *J. Med. Microbiol.* **35**, 23–28.

Murshudov, G. N., Skubák, P., Lebedev, A. A., Pannu, N. S., Steiner, R. A., Nicholls, R. A., Winn, M. D., Long, F. & Vagin, A. A. (2011). *Acta Cryst.* D**67**, 355–367.

Nurizzo, D., Mairs, T., Guijarro, M., Rey, V., Meyer, J., Fajardo, P., Chavanne, J., Biasci, J.-C., McSweeney, S. & Mitchell, E. (2006). *J. Synchrotron Rad.* **13**, 227–238.

Ogino, H., Uchiho, T., Yokoo, J., Kobayashi, R., Ichise, R. & Ishikawa, H. (2001). *Appl. Environ. Microbiol.* **67**, 942–947.

Otwinowski, Z. (1991). *Proceedings of the CCP4 Study Weekend. Isomorphous Replacement and Anomalous Scattering*, edited by W. Wolf, P. R. Evans & A. G. W. Leslie, pp. 80–86. Warrington: Daresbury Laboratory.

Pallarès, I., Bonet, R., García-Castellanos, R., Ventura, S., Avilés, F. X., Vendrell, J. & Gomis-Rüth, F. X. (2005). *Proc. Natl Acad. Sci. USA*, **102**, 3978–3983.

Panjikar, S., Parthasarathy, V., Lamzin, V. S., Weiss, M. S. & Tucker, P. A. (2005). *Acta Cryst.* D**61**, 449–457.

Panjikar, S., Parthasarathy, V., Lamzin, V. S., Weiss, M. S. & Tucker, P. A. (2009). *Acta Cryst.* D**65**, 1089–1097.

Rawlings, N. D., Barrett, A. J. & Bateman, A. (2012). *Nucleic Acids Res.* **40**, D343–D350.

Reichard, U., Büttner, S., Eiffert, H., Staib, F. & Rüchel, R. (1990). *J. Med. Microbiol.* **33**, 243–251.

Reichard, U., Léchenne, B., Asif, A. R., Streit, F., Grouzmann, E., Jousson, O. & Monod, M. (2006). *Appl. Environ. Microbiol.* **72**, 1739–1748.

Santelli, E., Liddington, R. C., Mohan, M. A., Hoch, J. A. & Szurmant, H. (2007). *J. Bacteriol.* **189**, 3290–3295.

Sarfati, J., Monod, M., Recco, P., Sulahian, A., Pinel, C., Candolfi, E., Fontaine, T., Debeaupuis, J.-P., Tabouret, M. & Latgé, J.-P. (2006). *Diagn. Microbiol. Infect. Dis.* **55**, 279–291.

Sheldrick, G. M. (2008). *Acta Cryst.* A**64**, 112–122.

Sirakova, T. D., Markaryan, A. & Kolattukudy, P. E. (1994). *Infect. Immun.* **62**, 4208–4218.

Terwilliger, T. (2004). *J. Synchrotron Rad.* **11**, 49–52.

Winn, M. D. *et al.* (2011). *Acta Cryst.* D**67**, 235–242.

Yeats, C., Rawlings, N. D. & Bateman, A. (2004). *Trends Biochem. Sci.* **29**, 169–172.

Yike, I. (2011). *Mycopathologia*, **171**, 299–323.